

See discussions, stats, and author profiles for this publication at: <https://www.researchgate.net/publication/259231666>

Flexible Coral-like Carbon Nanoarchitectures via a Dual Block Copolymer-Latex Templating Approach

ARTICLE *in* CHEMISTRY OF MATERIALS · NOVEMBER 2013

Impact Factor: 8.35 · DOI: 10.1021/cm4029676

CITATIONS

15

READS

116

4 AUTHORS, INCLUDING:



[Robin J White](#)

Fraunhofer Institute for Solar Energy Systems ...

49 PUBLICATIONS 2,186 CITATIONS

SEE PROFILE



[Maria-Magdalena Titirici](#)

Queen Mary, University of London

124 PUBLICATIONS 6,609 CITATIONS

SEE PROFILE

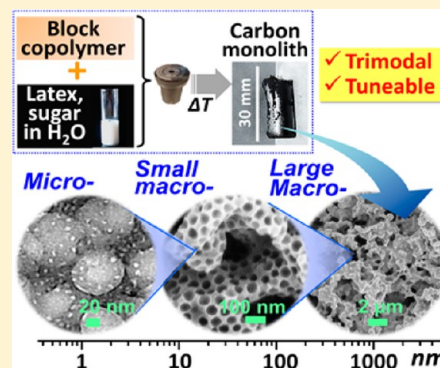
Flexible Coral-like Carbon Nanoarchitectures via a Dual Block Copolymer–Latex Templating Approach

Shiori Kubo,^{*,†} Robin J. White,[‡] Klaus Tauer,[§] and Maria-Magdalena Titirici^{||}[†]Department of Environmental Management Technology, National Institute of Advanced Industrial Science and Technology (AIST), 16-1, Onogawa, Tsukuba, Japan[‡]Institute for Advanced Sustainability Studies e.V. (IASS), Berliner Strasse 130, D-14467 Potsdam, Germany[§]Max-Planck Institute of Colloids and Interfaces, Am Muehlenberg 1, D-14476 Potsdam-Golm, Germany^{||}School of Engineering and Materials Science, Queen Mary University of London, Mile End Road, E1 4NS, London, United Kingdom

S Supporting Information

ABSTRACT: Novel, hierarchical, micro- (<2 nm), meso-/small macro- (50–60 nm), and large macro- (2–5 μm) trimodal porous functional carbon monoliths with flexible pore widths and wall textures are fabricated hydrothermally via a one-pot, dual block copolymer–latex templating approach. The trimodal carbon monoliths exhibit a coral-like nanoarchitecture, consisting of a 3D continuous carbon branch network, in which an inverse opal-type nanostructure with ordered pore wall texture is embedded, possessing high surface area (e.g., >800 $\text{m}^2 \text{g}^{-1}$), large pore volume, and highly layered porosities. The coadded block copolymer plays a triple role in the formation of the porous nanoarchitectures during hydrothermal synthesis: (1) in the formation of inverse opal pores by latex destabilization, (2) in the formation of an ordered microporous carbon wall texture by soft templating effect, and (3) in the formation of a micrometer-sized 3D continuous void by controlling the degree of spinodal phase separation. All the above nanostructuring chemistries are controllable via a simple variation in hydrothermal treatment temperature and reagent/template ratios offering nanostructural flexibility at multiple length scales, while the mild synthesis temperatures provide useful surface functionalities. The resulting materials are promising candidates for applications including (bio)electrochemistry (e.g., biofuel cells) or as biological scaffolds or separation media.

KEYWORDS: carbon, inverse opals, macroporous, mesoporous, microporous, hierarchical porosity, hydrothermal carbonization, soft templating, polystyrene latex, amphiphilic block copolymer, pluronics



1. INTRODUCTION

The “nanocasting” or “templating” of monodisperse nanoparticles (e.g., polystyrene latex (PSL) or colloidal silica) provides an opportunity to obtain uniform, (typically macro-) porous materials possessing spherically shaped regular pores. The selection of nanoparticle template size allows control of the pore dimension across the nano- and micrometer range. Manipulation of synthetic conditions leads to either individual hollow spheres¹ or interesting porous bodies termed “inverse opals.”² In the first case, the template surface is coated with a thin layer of the growing solid phase followed by removal of nanoparticles (e.g., via thermal decomposition, solvent extraction, or acid etching). Inverse opal structures are typically obtained via infiltration of nanoparticle interstices of aggregating spherical nanoparticles (i.e., the “opals”) with the precursor of choice followed by template removal procedures.

As compared to individual hollow spheres, whose use is often aimed specifically at delivery/protection of biologically/pharmaceutically important moieties (e.g., drugs,³ contrast imaging agents,⁴ and DNA⁵), deployment of such uniform

macropores into a continuous matrix of interest (i.e., production of inverse opal structures) opens up applications as photonic crystals,⁶ binder-free electrodes in secondary batteries,^{7,8} thermal insulators,⁹ or scaffold materials for large biomolecules (e.g., biochemical sensor electrodes¹⁰ and cell cultures¹¹), due to their well- and densely aligned and (large-diameter) uniform pore wall structures. For a successful fabrication of such “inverse opal” structures, the nanoparticles must closely pack in order to generate regularly aligned pore domains. Techniques for this include electrical/chemical deposition of nanoparticles on substrates, solvent evaporation of nanoparticle dispersion, and colloidal destabilization of nanoparticle dispersions.¹² At the same time, control of pore accessibility/interconnectedness/pore wall thickness/pore wall texture, is dependent on selection and optimization of those synthetic procedures. Promisingly from a viewpoint of materials

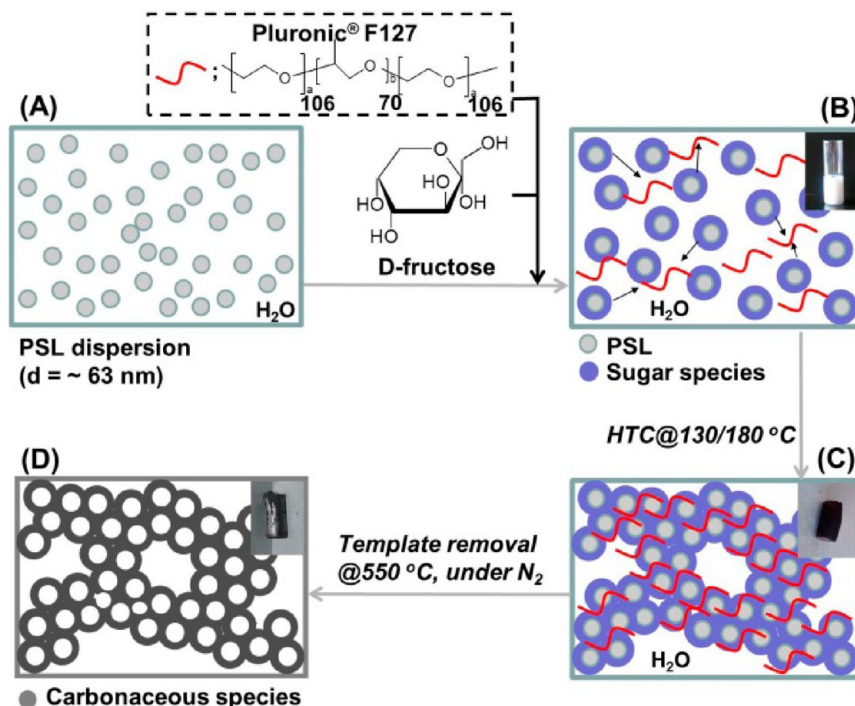
Received: September 4, 2013

Revised: November 10, 2013

Published: November 12, 2013



Scheme 1. Synthetic Strategy for the Fabrication of Coral-like Hierarchical, Trimodal Carbon Monolith; Insets in B, C, and D correspond to Optical Photographs of Synthesis Solution, Carbon Monolith before Template Removal, and Carbon Monolith after Template Removal, Respectively



morphology, inverse opal materials can be formed as monoliths,⁸ spheres,¹³ or films,¹⁴ composed of conjugated polymers,¹⁵ carbons,^{7,8,16} inorganic oxides,^{2,17} and metals.¹⁸

The synthesis of carbon inverse opals (CIOs) is of significant interest because of potentially high electrical and thermal conductivity and thermochemical/mechanical stability compared to polymeric and inorganic counterparts. Stein et al. demonstrated the synthesis of CIOs/metal oxides with pore diameters up to 300 nm and their use as electrodes in Li-ion batteries with good rate performance.⁸ Song et al. have also utilized similar CIO photonic crystals with a pore size of 200–300 nm as oil sensor devices.¹⁹ With regard to precursor selection and synthesis procedures, CIOs have traditionally been based on carbon aerogel precursor recipes (e.g., via using phenol-formaldehyde carbon precursors) or CVD methods (e.g., using hydrocarbon vapor precursors) and multistep processes (i.e., aggregation of nanoparticles by centrifugation/solvent evaporation followed by infiltration of carbon precursor(s) and occasionally followed also by template removal by acid etching),^{6b,16,20} while these procedures somewhat limit the tuneability of synthetic conditions and consequently of carbon pore wall thickness and textures. In addition, because of the chemical nature of the synthetic pathways employed, the resulting CIOs are rather chemically inert and homogeneous with regard to surface functionality, inhibiting further simple surface functionalization protocols.

With the aim of utilizing useful, preformed, naturally occurring structures for the fabrication of CIO's, Lu et al. recently reported the template-free synthesis of macroporous carbon using single cell fungi (i.e., yeast cell) as a carbon precursor and porogen.²¹ However, the obtained structures are not well-defined and are rather heterogeneous in size and shape uniformity. For the successful use of CIOs in the aforementioned applications, it would be desirable to develop a synthetic

platform that allows relatively simple access to flexible pore wall chemistry and controlled, inverse opal nanostructures (i.e., controlled pore width, pore wall thickness/texture, pore accessibility/interconnectedness, and external morphology of inverse opal nanostructures).

In this context, hydrothermal carbonization (HTC) is a sustainable synthetic route toward functional carbonaceous materials via a mild, aqueous, one-pot approach utilizing renewable carbon precursors (e.g., carbohydrates, biomass).²² The applicability of HTC in the preparation of a wide range of tunable porous structures and material morphologies by the use of additives/templates highlights another significant synthetic advantage.²³ The production of ordered micro/mesoporous carbon²⁴ and functional (i.e., nitrogen-doped) carbonaceous aerogels²⁵ has been recently reported. We have also previously reported on the preparation of functional hollow carbon nanospheres via the HTC of a model saccharide (e.g., D-glucose), in the presence of monodisperse PSL templates.²⁶ Such hollow nanocarbons are potential encapsulation agents (e.g., in drug delivery systems), while they were also found to serve as excellent electrode materials in Na- and Li-ion batteries.²⁷

In this paper, we take advantage of the PSL templating and extend the approach toward the preparation of hierarchical, trimodal porous carbon monoliths with inverse opal-type structures and with flexible porous properties via PSL templating mediated by an amphiphilic block copolymer (i.e., Pluronic F127, EO₁₀₆PO₇₀EO₁₀₆). The addition of the block copolymer (1) destabilizes the PSL during the HTC process and induces close packing,²⁸ (2) introduces additional ordered porous texture into the forming carbon walls via a soft templating effect (Scheme 1A–C),^{24,26} and (3) controls phase separation kinetics during HTC (i.e., via controlling the degree of spinodal-type phase separation), similar to the mechanism

described in both templated and nontemplated polymerization/sol–gel systems²⁹ and introduces a micrometer-sized 3D continuous carbon branch nature. By benefiting from the temperature/concentration dependency of all the above effects offered by the block copolymer, we aim to introduce an approach to access the carbon inverse opal-type nanostructures with hierarchical and flexible nanoarchitectures (i.e., tunable pore wall thickness/texture, width of 3D continuous carbon intrabranch void).

This paper is constructed as follows: First, we demonstrate the synthesis and nanostructure tuning of the hierarchical, coral-like carbon monoliths via selecting two different HTC temperatures (i.e., 130 and 180 °C, designated as T_{HTC}). This temperature variation controls the block copolymer adsorption on the PSL surface (i.e., control in the degree of aggregation) as well as the spinodal phase separation kinetics (i.e., control in the larger, micrometer-scale morphology) and concurrently dictates block copolymer (micellar) stability in the presence of PSL (i.e., control in soft templating effect and thus in the pore wall texture). The utilized block copolymer was previously reported to be stable (i.e., formation of stable micelles observed) during HTC at 130 °C and unstable at 180 °C (i.e., loss of ordered micellar domains).²⁴ Second, the T_{HTC} was kept constant (i.e., $T_{\text{HTC}} = 180$ °C), while the block copolymer concentration (C_{polymer}) was varied to allow further demonstration of structure tuneability as well as to elucidate the effect of the added block copolymer on the formation of the hierarchical, coral-like nanoarchitectures. Each synthesis was accompanied by a final carbonization/template thermolysis step (Scheme 1D). D-Fructose (Fru) was selected as a carbon precursor allowing the use of a $T_{\text{HTC}} = 130$ °C.²⁴

2. EXPERIMENTAL SECTION

Chemicals. Hydroxyl-terminated polystyrene latex aqueous dispersion ($d_n \approx 63$ nm, 19 wt % aqueous solution, wherein d_n corresponds to peak diameter in size distribution by number) was synthesized via a procedure described elsewhere.³⁰ D-Fructose was purchased from Wako Chemicals. Pluronic F127 was purchased from Sigma-Aldrich. All chemicals were used without further purification.

Synthesis Method. In a typical synthesis, 0.25 g of Pluronic F127 ($M_w = 12\,500$, EO₁₀₆-PO₇₀-EO₁₀₆) and 2.4 g of D-fructose were dissolved in 8 mL of distilled water. A total of 2 mL of the PSL dispersion was then added followed by vigorous stirring at room temperature for 10 min. The system was heat-treated either at 130 °C for 120 h or at 180 °C for 48 h in a stainless autoclave (Paar, Acid digestion vessel). After reaction, the obtained carbon monolith was washed with excess distilled water and ethanol and dried at 65 °C overnight. The polymer templates were removed by calcination under N₂ either at 550 °C or at 900 °C for 4 h. For comparison purposes, a block copolymer concentration was varied from 0.5 to 5.0 wt % stepwise under HTC at 180 °C followed by the same washing and calcination steps.

Characterization Techniques. Field-emission scanning electron microscopy (FE-SEM) was performed on a HITACHI S-4700. Thermogravimetric Analysis (TGA) was performed using a Rigaku Thermoplus TG 8120 over a temperature range from room temperature to 1000 °C at a heating rate of 10 K min⁻¹ and under a nitrogen flow of 200 mL min⁻¹. Elemental compositions were determined using CE Instruments EA1110. X-ray Photoelectron Spectroscopy (XPS) was performed using Escalab220i-XL (Fisons Instruments) with Cu K α radiation. X-Ray Diffraction (XRD) patterns were recorded on Rigaku SmartLab with Cu K α at a scan rate of 2° min⁻¹. Transmission Electron Microscopy (TEM) images were acquired using a Topcon EM-002B with an acceleration voltage of 120 kV. Small Angle X-ray Scattering (SAXS) patterns were recorded on Rigaku SmartLab with Cu K α with the SAXS attachment at a scan

rate of 0.26° min⁻¹. Mercury (Hg) porosimetry was performed with AutoPore IV 9500, V 1.09 (Micrometrics). N₂ and CO₂ gas sorption analyses were carried out using Belsorp max at 77 K and Belsorp 28 (Nippon Bel Co.) at 298 K, respectively. Specific conductivity measurements were carried out with Loresta GP MCP-T610 resistivity meter equipped with four-pin probe (Mitsubishi Chemicals Analytech Co.) and with the built-in calculation software. Zeta potential measurement was carried out at a solution temperature of 25 °C using an ELSZ-1000 from Otsuka Electronics Co., with a detection angle of 15°. Please see the Supporting Information for further characterization details.

3. RESULTS AND DISCUSSIONS

3.1. Structural Control by Variation of T_{HTC} . The HTC of Fru in the presence of PSL and F127 at 130 °C yielded a monolithic composite (Figure 1A inset, see Figure S1 in the Supporting Information for TEM of the native PSL nanoparticles). SEM image analysis of this composite revealed the successful close packing of hydrothermal carbon-coated PSL nanoparticles (Figure 1A). Thermal gravimetric analysis (TGA) of the composite material performed under N₂ indicated two main decomposition events namely at 359 and 418 °C (see Figure S2A in the Supporting Information). The former was attributed to the decomposition of F127, while the latter was attributed to the PSL component.^{24,26} The synthesis at T_{HTC} of 180 °C also yielded monolithic-like material with a higher degree of PSL close packing (Figure 1B and inset), while again showing two decomposition peaks at 382 and 423 °C in the differential TGA curve (Figure S2B; a slightly higher second decomposition event was attributed to an increased stability of the formed HTC phase as a result of processing at 180 °C). To completely remove both polymeric templates, thermal treatment under a N₂ atmosphere was performed at 550 °C.

After template removal, the monolithic form was maintained in both examples (Figure 1C and D insets). Elemental analysis of the material prepared at a T_{HTC} of 130 °C thermally treated at 550 °C (designated as $T_{\text{HTC}}_{130/550}$) revealed the synthesis of a carbon-rich material composed of C (88.4%), H (2.4%), and O (9.2%) (Table 1), whereas XPS analysis indicated surface functional groups of hydrothermal carbons prepared at this temperature (e.g., C–O–, C=O– functionalities; Figure S3A and Table S1 in the Supporting Information),^{24,26,31} advantageous for possible further surface functionalization of this monolithic carbon phase. The material prepared at 180 °C followed by calcination at 550 °C (designated as $T_{\text{HTC}}_{180/550}$) also possessed oxygenated surface functional groups (see Figure S3B and Table S1 in the Supporting Information) and was composed of C (90%), H (2.3%), and O (7.5%) (Table 1), whereas in both cases, the carbon network represented amorphous features as indicated by wide-angle XRD patterns (i.e., the presence of two broad peaks at $2\theta \approx 22$ and 43° ; see Figure S4A, B in the Supporting Information).

SEM analysis of the resulting monoliths revealed coral-like structures, with a hierarchical macroporosity composed of large 3D continuous carbonaceous branches, in which the inverse opal-type nanostructure is embedded (Figure 1C–F). The overall skeleton thickness was found to be thinner for $T_{\text{HTC}}_{130/550}$ (0.5–1 μm , Figure 1E) as compared to $T_{\text{HTC}}_{180/550}$ (2–4 μm , Figure 1F), whereas the width of the 3D continuous intrabranch void (designated as d_{3D}) was found to also differ between the two materials ($d_{3D} = 1$ –2 μm for $T_{\text{HTC}}_{130/550}$ and 3–4 μm for $T_{\text{HTC}}_{180/550}$). The diameter of the inverse opal-type spherical pores (designated as d_{sp}) formed by the decomposition of PSL and carbon wall

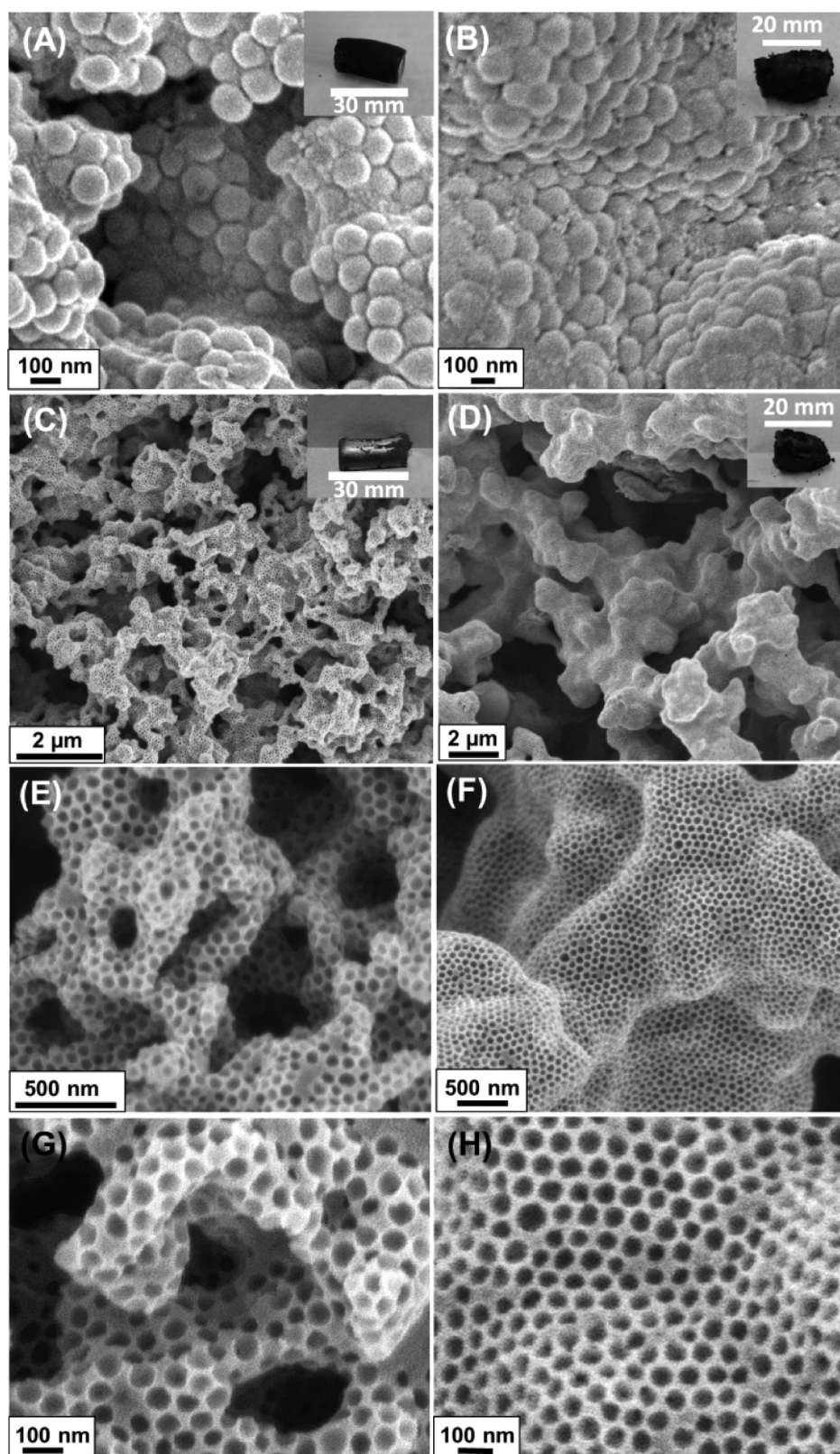


Figure 1. SEM micrographs of a coral-like porous carbon monolith synthesized at a T_{HTC} of (left column) 130 °C and (right column) 180 °C. A and B correspond to monoliths before template removal; C, E, and G to $T_{\text{HTC}}_{130/550}$ (i.e., after template removal); and D, F, and H to $T_{\text{HTC}}_{180/550}$ (i.e., after template removal). Each inset represents an optical photograph of each corresponding carbon monolith.

shrinkage was found to be between 50 and 60 nm region in both cases (Figure 1G, H), whereas TEM revealed that the

whole carbon skeleton was composed of inverse opal-type structures (see Figure S5A, B in the Supporting Information).

Table 1. Summary of Pore Properties and Elemental Compositions of the Synthesized Coral-Like, Hierarchical Trimodal Carbon Monoliths

sample name ^a	V_{Hg}^b [cm ³ g ⁻¹]	$d_{3\text{D}}, d_{\text{sp}}^b$	S_{BET}^c [m ² g ⁻¹]	$V_{\text{total},\text{N}_2}^d$ [cm ³ g ⁻¹]	$V_{\text{meso-macro},\text{N}_2}^e$ [cm ³ g ⁻¹]	$V_{\text{micro},\text{N}_2}^f$ ($V_{\text{micro},\text{CO}_2}^g$) [cm ³ g ⁻¹]	d_{BJH}^h	elemental composition [%]		
								C	H	O
$T_{\text{HTC}}_{130/550}$	4.03	2.4 μm , 54 nm	621	0.90	0.66	0.24 (0.39)	58 nm	88.4	2.4	9.2
$T_{\text{HTC}}_{180/550}$	2.34	3.3 μm , 60 nm	634	1.00	0.77	0.23 (0.39)	55 nm	90.2	2.3	7.5
$T_{\text{HTC}}_{130/900}$	3.59	2.2 μm , 53 nm	823	0.93	0.60	0.33 (0.68)	60 nm	88.9	1.1	10
$T_{\text{HTC}}_{180/900}$	2.20	2.7 μm , 64 nm	520	0.66	0.46	0.20 (0.50)	53 nm	93.8	0.3	5.9

^aSample names, in which the first and the second temperatures correspond to T_{HTC} and post heat treatment temperature, respectively. ^bCumulative intrusion volume and peak positions of pore size distributions as determined by Hg porosimetry. ^cBET surface area as determined by N₂ sorption.

^dTotal pore volume as determined by N₂ sorption isotherms. ^eMeso-/small macropore volume as calculated from the N₂ sorption adsorption branch of the region corresponding to $d > \sim 2.4$ nm using the BJH method. ^fMicropore volume calculated by subtracting $V_{\text{meso-macro},\text{N}_2}$ from $V_{\text{total},\text{N}_2}$.

^gMicropore volume as determined by CO₂ sorption isotherms. ^hPore diameter calculated by BJH model.

Through a closer examination of the carbon wall of the inverse opal structure for $T_{\text{HTC}}_{130/550}$, an ordered pore system was observed within the micro/small mesopore range, with a pore-to-pore distance of ~ 10 nm (Figure 2A, inset). This ordered texture indicates a soft templating effect of the added block copolymer and the generation of an ordered lyotropic phase. In contrast, in the case of $T_{\text{HTC}}_{180/550}$, because of the instability of the F127 lyotropic phase at this higher T_{HTC} , no ordered micro/mesopore structure was observed during TEM image analysis (Figure 2B). Complementarily, in the SAXS pattern of the $T_{\text{HTC}}_{130/550}$ material, a peak was observed at $q = 0.54$ nm⁻¹, corresponding to a d -spacing of 11.6 nm (i.e., thus, in good agreement with the observed pore-to-pore distance in TEM), confirming further a soft templating effect. No peak was observed in the SAXS pattern for $T_{\text{HTC}}_{180/550}$ (Figure 2C). Because of this lack of an ordered lyotropic phase at the PSL surface at a T_{HTC} of 180 °C, an enhanced close packing of the PSL nanoparticles was induced, resulting in a thinner carbon wall (ca. 5–10 nm, Figure 2B) compared to the $T_{\text{HTC}}_{180/550}$ material (ca. 20–30 nm, Figure 2A).

Presumably, during the HTC synthesis, the amphiphilic block copolymer promotes aggregation of PSL as well as phase separation via a spinodal-type decomposition²⁹ occurring between the water-rich and block copolymer/carbon-rich phases. Carbonization proceeds in the interstices of the forming aggregates, effectively “trapping” the formed nanostructures, whereas interactions between a block copolymer and Fru as well as the hydrophilic surface of PSL and Fru (e.g., via hydrogen bonding) serve as the major templating driving force. At a T_{HTC} of 130 °C, the block copolymer presumably exists as micelles loosely adsorbed at the PSL surface,³² providing the carbon wall with an ordered porous texture. At a T_{HTC} of 180 °C, the stronger tendency for block copolymer adsorption as well as micelle instability leads to an increased PSL aggregation and a loss in the ordered pore system in the carbon wall of the inverse opal nanostructure. The observed difference in the carbon branch thickness as well as in the width of the carbon intrabranched void (i.e., $d_{3\text{D}}$) is proposed to be related to the difference in the degree of spinodal-type phase separation at the two T_{HTC} 's investigated.²⁹ Thus, our procedure provides access to inverse opal-type carbon solids with the nanostructures controllable at multiple length scales; the pore wall texture/thickness, carbon skeleton thickness, and dimension of intrabranched void can be directed simply by varying T_{HTC} , whereas inverse opal structuring of the carbon skeleton results from PSL destabilization.

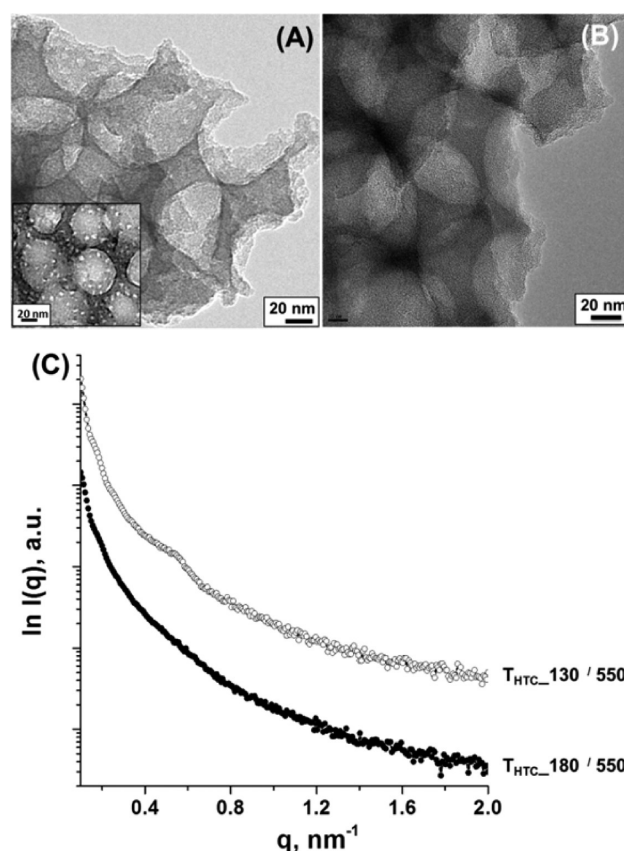


Figure 2. TEM micrographs of the coral-like trimodal carbon monolith (A) $T_{\text{HTC}}_{130/550}$ and (B) $T_{\text{HTC}}_{180/550}$ (i.e., after template removal). (C) Small-angle X-ray scattering (SAXS) patterns of coral-like trimodal carbon monoliths.

These coral-like carbon nanoarchitectures were found to possess large macro-, meso/small macro-, and microtrimodal porosities, which was revealed by a combination of Hg intrusion porosimetry and N₂ and CO₂ gas sorption analyses. Hg intrusion porosimetry generated two peaks at pore diameters of ~ 2.4 μm and ~ 56 nm respectively for $T_{\text{HTC}}_{130/550}$ contributing to a cumulative intrusion volume (designated as V_{Hg}) of 4.03 cm³ g⁻¹ (Figure 3A, B, Table 1). Through comparison with the obtained electron microscopy images (Figure 1C, E, G), the larger pore diameter can be attributed to $d_{3\text{D}}$ and the smaller to d_{sp} , depicting both the favorable replication of the PSL aggregates and the uniformity

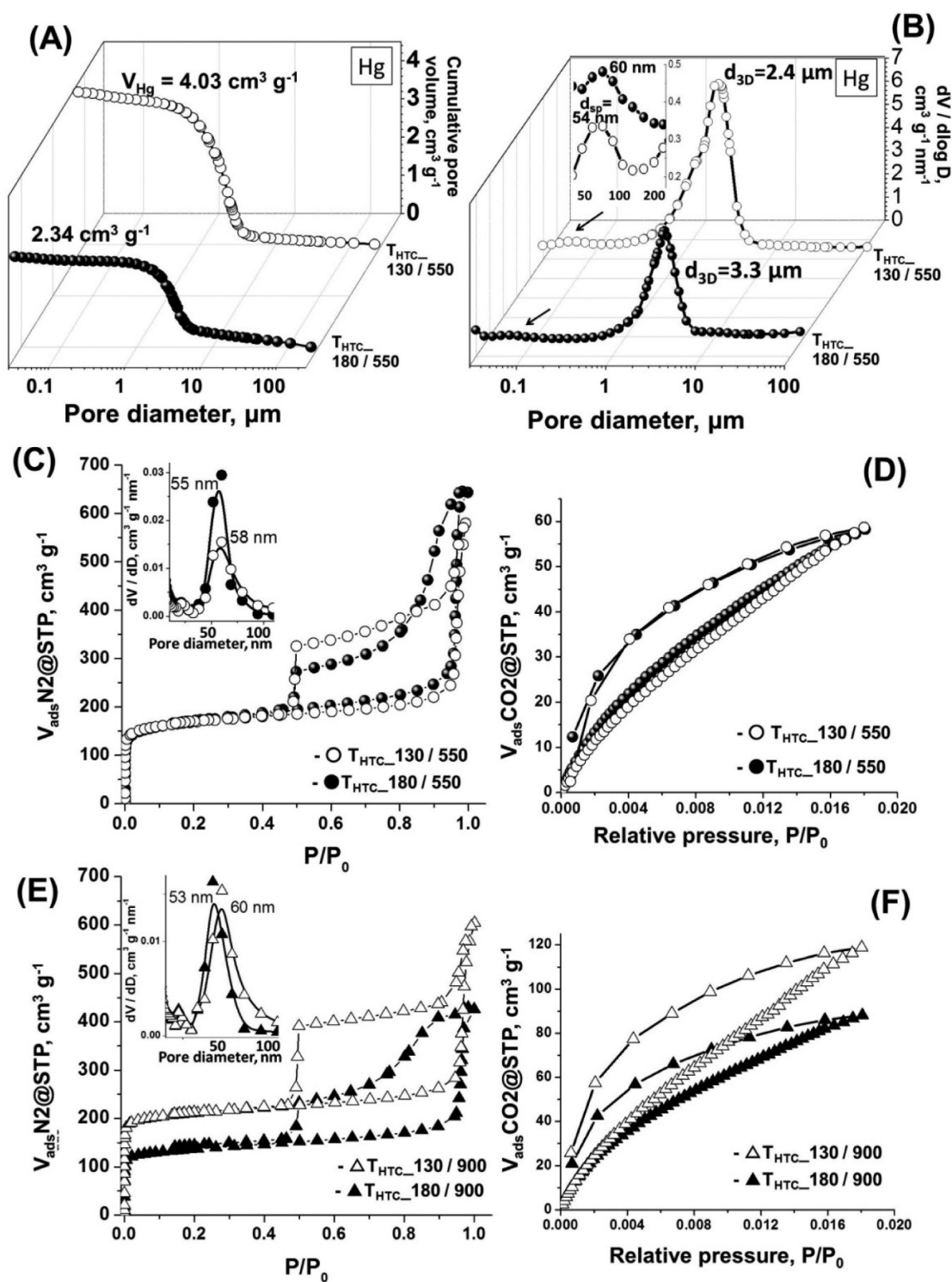


Figure 3. (A) Hg cumulative intrusion volume, (B) Hg intrusion pore size distribution (inset, enlarged pore size distributions of the range pointed by arrows), (C) N_2 sorption isotherms (with inset showing BJH pore size distributions), and (D) CO_2 sorption isotherms of the hierarchical trimodal coral-like carbon monolith $T_{HTC_130/550}$ (○) and $T_{HTC_180/550}$ (●). (E) N_2 sorption isotherms (with inset showing BJH pore size distributions) and (F) CO_2 sorption isotherms of the hierarchical coral-like carbon monolith $T_{HTC_130/900}$ (△) and $T_{HTC_180/900}$ (▲).

of the width of the formed 3D continuous carbon intrabranch void. Note that d_{sp} peaks appear to be small in spite of the fact that the whole carbon skeleton is composed of inverse opal-type structuring. This can be explained by the fact that in Hg intrusion analysis for inverse opals with the diameter of d_{sp} , only the pores located at the outer surfaces can be filled at the given corresponding intrusion pressure.³³ A marked shift of the

d_{3D} peak to $\sim 3.3 \text{ }\mu\text{m}$ was observed for $T_{HTC_180/550}$, whereas the position of the d_{sp} peak was comparable to $T_{HTC_130/550}$ (i.e., $\sim 60 \text{ nm}$ with V_{Hg} of $2.34 \text{ cm}^3 \text{ g}^{-1}$, Figure 3A, B, Table 1). This further confirms that the variation in T_{HTC} contributes to controlling the width of the carbon intrabranch void (i.e., d_{3D}), whereas the inverse opal-type structure is maintained.

N₂ sorption yielded type IV, micro/meso porous isotherm features with a total pore volume of 0.90 cm³ g⁻¹ for $T_{\text{HTC}}_{130/550}$ and 1.00 cm³ g⁻¹ for $T_{\text{HTC}}_{180/550}$, respectively (Figure 3C, Table 1). Complementary to the d_{sp} dimension analyzed by electron microscopy and Hg porosimetry (Figure 1G, H and Figure 3B inset), the BJH pore size distributions generated the peak centered at ~58 nm for $T_{\text{HTC}}_{130/550}$ and ~55 nm for $T_{\text{HTC}}_{180/550}$, contributing to the sharp N₂ uptake of 0.66 and 0.77 cm³ g⁻¹ at $P/P_0 \approx 0.9$ (i.e., designated as $V_{\text{meso-macro},\text{N}_2}$; Table 1, Figure 3C inset). Hysteresis loop profiles typical of ink-bottle-shaped pore morphology were observed for both cases as a result of the filling of pores generated from the removal of the PSL template and associated macropore connectivity induced from block copolymer template removal from the spherical pore walls.^{34,35}

Micropore volume was calculated as 0.24 cm³ g⁻¹ for $T_{\text{HTC}}_{130/550}$ and 0.23 cm³ g⁻¹ for $T_{\text{HTC}}_{180/550}$, respectively (Table 1, designated as $V_{\text{micro},\text{N}_2}$), contributing to approximately 25% of the total pore volume, generated as a result of the block copolymer template removal coupled with concurrent decomposition of the HTC carbon matrix.³⁶ The microporosity further quantified via CO₂ sorption at 298 K yielded a micropore volume (designated as $V_{\text{micro},\text{CO}_2}$) of ~0.39 cm³ g⁻¹ for both materials (Figure 3D, Table 1). The higher $V_{\text{micro},\text{CO}_2}$ value as compared to $V_{\text{micro},\text{N}_2}$ for both cases indicates the existence of small micropores, not (kinetically) accessible to the N₂ probe adsorbate in these materials. In this manner, flexible, highly layered porosities in the pore size regime of micro (<ca. 2 nm), inverse opal-type meso/small macro- (ca. 50–60 nm) and large macro- (2.4–3.3 μm) pores were revealed. No observed significant difference in microporosity between $T_{\text{HTC}}_{130/550}$ and $T_{\text{HTC}}_{180/550}$ might be derived from a possible “closed pore” nature of the block copolymer-templated pores of $T_{\text{HTC}}_{130/550}$ at this stage.

With the aim of providing the materials with electrical conductivity important from an application point of view, thermal treatment at 900 °C (under N₂) was performed (these monoliths are designated as $T_{\text{HTC}}_{130/900}$ and $T_{\text{HTC}}_{180/900}$ depending on T_{HTC}). Elemental analysis revealed an increase in carbon content for both materials, with a comparatively high O content for $T_{\text{HTC}}_{130/900}$ (i.e., ~10%, Table 1). This may be due to the leaving of less stable species (e.g., CH₄ from –CH₃ or methylene bridge)^{36–38} from less condensed, flexible carbonaceous structures in material prepared at 130 °C—the lower HTC processing temperature generating potentially differing carbonization pathways and final material chemistry. For both materials, due to the increase in the degree of aromatization/graphitization of the forming carbon network, as demonstrated by increasingly resolved X-ray diffraction peaks at $2\theta = 23$ and 44° (see Figure S4C, D in the Supporting Information) and a corresponding increase in sp² hybridization (i.e., increase in peak area by 7% in C1(s) XPS analysis; see Figure S3C, D and Table S1 in the Supporting Information),³⁹ promising electrical conductivities of 30 S m⁻¹ for $T_{\text{HTC}}_{130/900}$ and 11 S m⁻¹ for $T_{\text{HTC}}_{180/900}$ were found (i.e., as compared to 160 S m⁻¹ for commercial carbon conductive additive measured by the same method⁴⁰). The higher conductivity of $T_{\text{HTC}}_{130/900}$ may be due to a higher graphitization degree, as indicated by the improved resolution of XRD peaks, potentially the result of differing carbonization pathways between $T_{\text{HTC}}_{130/900}$ and $T_{\text{HTC}}_{180/900}$ (see Figure S4C, D in the Supporting Information). Additionally,

the thicker carbon wall feature of $T_{\text{HTC}}_{130/900}$ may also positively contribute to increased conductivity, while the contribution of the 3D branch thickness (i.e., larger for $T_{\text{HTC}}_{180/900}$) was found to be comparably minor. The monolithic external morphology as well as hierarchical pore structuring of 3D continuous intrabranch void and inverse opal-type structure were found to be stable after thermal treatment at 900 °C under N₂ (see Figure S6A–F in the Supporting Information) presenting practically identical d_{sp} and V_{Hg} values to that of $T_{\text{HTC}}_{130/550}$ and $T_{\text{HTC}}_{180/550}$ (i.e., ~53 nm and 3.59 cm³ g⁻¹ for $T_{\text{HTC}}_{130/900}$ and ~64 nm and 2.20 cm³ g⁻¹ for $T_{\text{HTC}}_{180/900}$; Table 1, Figure S7A, B in the Supporting Information).

Significantly, in contrast to the maintainance of d_{sp} and V_{Hg} values, carbonization at 900 °C increased $V_{\text{micro},\text{N}_2}$, particularly for $T_{\text{HTC}}_{130/900}$ (i.e., from 0.25 to 0.33 cm³ g⁻¹ with the increase in S_{BET} from 661 to 823 m² g⁻¹, Figure 3E, Table 1). Interestingly, for $T_{\text{HTC}}_{180/900}$, $V_{\text{micro},\text{N}_2}$ was found to decrease marginally (i.e., from 0.23 to 0.20 cm³ g⁻¹/ S_{BET} from 634 to 520 m² g⁻¹; Figure 3E, Table 1, see Figure 3E inset for BJH pore size distributions), illustrating the distinct difference from $T_{\text{HTC}}_{130/900}$. The observed increasing trend of porosity for $T_{\text{HTC}}_{130/900}$ is believed to be derived from the increased accessibility to block copolymer-templated micro/small mesopores after carbonization at 900 °C, which was offered as a consequence of carbon structure transformation (i.e., carbon sheet reordering/further carbon wall condensation), whereas it renders the pore ordering less regular (see TEM and SAXS pattern with peak broadening at $q \approx 0.58$ nm⁻¹, in Figure S8 in the Supporting Information).³⁹ Nevertheless, in terms of $V_{\text{micro},\text{CO}_2}$ a large increase was observed for both materials (i.e., from 0.39 to 0.68 cm³ g⁻¹ for $T_{\text{HTC}}_{130/900}$ because of the soft templating effect and from 0.39 to 0.50 cm³ g⁻¹ for $T_{\text{HTC}}_{180/900}$ occurring due to the reordering of carbon sheets creating very small micropores such as ultramicropores, kinetically accessible only by CO₂ (Figure 3F).³⁶ The combination of useful electrical conductivity and highly layered porosity potentially renders these materials suitable as porous conductive carbon electrodes/supports for (bio)-electrochemistry (e.g., biofuel cells).

3.2. Structural Control by Variation of the Block Copolymer Concentration (C_{polymer}). As a further demonstration of structure tuneability accessible via our presented synthetic approach and to unravel the influence of the block copolymer (i.e., F127) on the observed material properties, the C_{polymer} in synthesis solution was varied. Other synthetic parameters were kept constant, while a T_{HTC} of 180 °C was used to simplify the synthetic systems (i.e., by ruling out the soft templating effect) and to allow the clear-cut observations regarding the role of F127. A zeta potential investigation was also performed to allow a degree of prediction regarding PSL colloidal stability in solution with relation to C_{polymer} .

SEM image analysis of the monolithic materials prepared at varied C_{polymer} values (i.e., from 0.5 to 5.0 wt % in a stepwise manner, with the absolute amount of PSL and Fru kept constant) revealed an increase in carbon branch thickness from <1 μm to ca. 4 μm as C_{polymer} increases (Figure 4A–D). The $d_{3\text{D}}$ as measured by Hg porosimetry was found to also gradually increase from approximately 1.3 to 4.7 μm (i.e., with V_{Hg} decreasing from 9.70 to 1.72 cm³ g⁻¹, see Figure S9A, B in the Supporting Information), demonstrating a degree of tuneability of both carbon branch thickness and $d_{3\text{D}}$ via the variation in

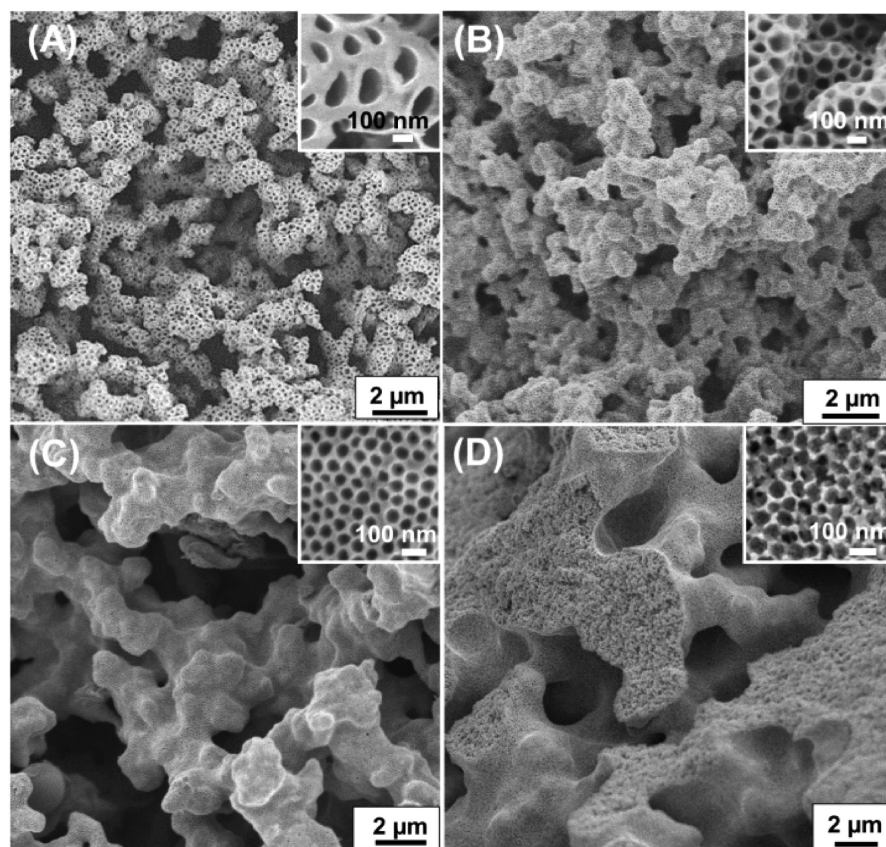


Figure 4. (A–D) SEM micrographs of the materials prepared at 180 °C at varied F127 concentration (C_{polymer}) of 0.05, 1.3, 2.5, and 5.0, respectively (each inset corresponds to a SEM micrograph taken at higher magnification to allow careful observation of each branch nanostructure).

C_{polymer} (i.e., controllability in the degree of spinodal-type phase separation²⁹). The observed non-smooth shoulder natures for the materials prepared at $C_{\text{polymer}} = 0.5$ and 1.3 might possibly be due to decreased branch interconnectivity as reported for the Hg porosimetry of some silica gels with decreased 3D branch connectivity,⁴¹ whereas a partial collapse of the carbon branch during Hg intrusion cannot be discounted.

Dependence of the C_{polymer} on the formation of the PSL-templated nanostructure was found to be rather complex. At a C_{polymer} of 0.5 wt %, the pore size was observed to double that of the native PSL (Figure 4A, inset), generating a peak centered at ~ 136 nm in Hg porosimetry pore size distribution (see Figure S9i inset in the Supporting Information). Increase in C_{polymer} to 1.3 and 2.5 wt % resulted in the successful generation of inverse opal-type nanostructures indicated by the evolution of small d_{sp} peaks at 63 and 59 nm (see Figure S9ii and iii insets in the Supporting Information). In both cases, this was found to be in accordance with the SEM image analysis, where spherical pores were observed with the same dimension as the PSL template (Figure 4B and C insets). A further increase in C_{polymer} to 5.0 resulted in pore wall distortion and an increase in the random nature of the macropore interconnectivity (Figure 4D inset), resulting in removal of the d_{sp} peak (see Figure S9iv inset in the Supporting Information). Thus, the formation of a near-perfect inverse opal structure was found to be restricted to a C_{polymer} between 1.3 and 2.5, whereas 3D continuous voids with tunable width and branch thickness were accessible at all C_{polymer} investigated.

Zeta potential measurements revealed that the surface of the native PSL was highly negatively charged, showing a zeta

potential value of -25.6 mV (i.e., at a C_{polymer} of 0, Figure 5), whereas a decreasing trend in surface negativity was observed with a gradual increase in C_{polymer} (i.e., gradual decrease in zeta potential from -25.6 to -4.4 mV upon the increase in C_{polymer} from 0 to 5.0). This suggests that increasing C_{polymer} leads to an increased coverage of the PSL surface while contributing to competing 2-fold effects: elimination of electrostatic repulsion and sterical separation of adjacent PSL particles.

At a C_{polymer} of 0.5 wt %, surface coverage of PSL can be considered to be still relatively low, which may lead to collision and coalescence of two adjacent PSL particles or to the formation of PSL doublets by block polymer bridging (Figure 5, inset A).^{42,43} Thus, the formation of double-sized pores resulted. When increasing C_{polymer} to 1.3 and 2.5 wt %, respectively, adsorbed block copolymers are considered to play an effective role in sterically separating individual PSL (Figure 5, inset B), whereas the aggregation can be enhanced at the same time due to the decrease in their surface charge upon polymer adsorption (i.e., with the zeta potential values of -3.8 and -4.4 mV, respectively). Thus, these synthesis conditions are believed to provide an optimal aggregation state for the generation of inverse opal-type carbonaceous structures. At a C_{polymer} of 5.0 wt %, the further decrease in negativity of the zeta potential (i.e., to -1.2 mV, Figure 5, inset C) possibly results in eliminating electrostatic repulsion forces (i.e., “screened” repulsion).⁴³ Thus, because of the resulting closest particle–particle distance, inverse opal-type structures with interconnected and also distorted spherical pores were found to generate.

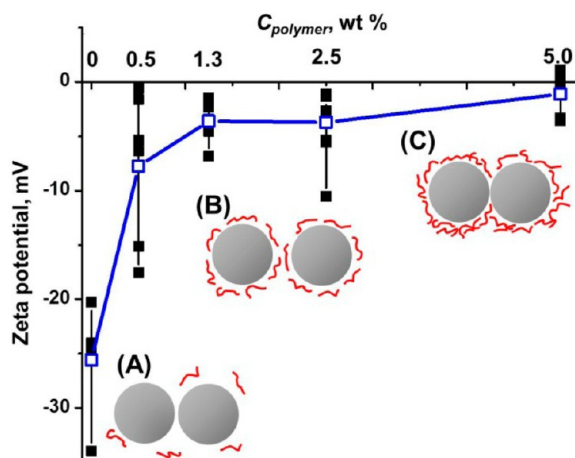


Figure 5. Measured (black square) and averaged ζ potentials (blue line) of PSL nanoparticles as a function of block copolymer concentration (C_{polymer}). Schematic illustrations A, B, and C correspond to interactions between PSLs (gray circle) at each C_{polymer} (red lines represent F127 block copolymer).

The use of a block copolymer at varied T_{HTC} (i.e., of 130 and 180 °C) and with a varied amount (i.e., from 0.5 to 5.0 wt %) was found to be an effective and powerful tool to access inverse opal-type carbon nanostructures with tunable pore wall textures/thicknesses with tunable 3D continuous branch voids and highly layered porosities. On the basis of this synthesis approach, further variation in the type of PSL template (e.g., different sizes/shapes) and/or block copolymer structure, besides synthesis temperature and composition, will provide extended tuneability regarding pore size/shape/connectivity and wall thickness/textures—features which play crucial roles in directing material properties for specific applications such as (binder-free) electrode materials, separation media, or scaffold materials (e.g., of biological moieties).^{8,16c} Further optimization of the 3D continuous carbon branch network structure will lead to an enhanced mass flow, rendering the materials suitable particularly for liquid-phase applications such as liquid-phase separation or as biofuel cells or biosensors.⁴⁴ The simplicity of the presented synthetic platform should be emphasized with specific reference to other systems based on inorganic templates, hazardous template removal steps,^{6b,20d} and multi-step protocols.^{20a–c}

4. CONCLUSIONS

We have presented the one-pot, tunable synthesis of novel, hierarchical, trimodal functional carbon monoliths with inverse opal-type structures and tunable wall texture via a facile, dual block copolymer–latex templating approach. The produced materials were found to possess coral-like nanoarchitectures with highly layered 3D continuous macro- (2–5 μm), spherical meso/small macro- (50–60 nm), and carbon wall micro- (<2 nm) porosities with high surface area and large pore volume. The addition of the block copolymer plays a significant role in controlling both colloidal PSL aggregation and the soft templating effect, while also contributing to tuning the degree of the observed spinodal-type phase separation. This is an elegant and flexible synthesis platform to produce interesting monolithic carbon-based nanostructures, in which uniform, flexible, and layered pore systems are deployed into a continuous carbon body simply by using a block copolymer additive. The trimodal porous features with flexible nanostruc-

ture and surface chemistry lend the synthesized structures to applications where a combination of enhanced mass flow, high pore volume/accessibility, and (dual) size/surface selectivity is highly desirable, and as such the presented materials hold promise in liquid-phase applications potentially as conductive electrodes in (bio)electrochemistry (e.g., as biofuel cells), separation media, or as scaffold materials (e.g., of biological moieties).

■ ASSOCIATED CONTENT

Supporting Information

Details of characterization methods and additional characterization data (electron micrographs, XPS, XRD, X-ray scattering, and Hg porosimetry). This material is available free of charge via the Internet at <http://pubs.acs.org>.

■ AUTHOR INFORMATION

Corresponding Author

*E-mail: kubo-shiori@aist.go.jp.

Notes

The authors declare no competing financial interest.

■ ACKNOWLEDGMENTS

The authors acknowledge Dr. Y. Soneda and Ms. M. Jona for SEM operation and Dr. N. Yoshizawa and Mr. Takatsuki for support in TEM. Dr. H. Takagi is greatly acknowledged for support in gas sorption. Dr. T. Sano is thanked for support in XPS analyses.

■ REFERENCES

- (1) Caruso, F.; Caruso, R. A.; Moehwald, H. *Science* **1998**, 282, 1111.
- (2) (a) Wijnhoven, J. E. G.; Vos, W. L. *Science* **1998**, 281, 802. (b) Velze, O. D.; Jede, T. A.; Lobo, R. F.; Lenhoff, A. M. *Nature* **1997**, 389, 447. (c) Holland, B. T.; Blanford, C. F.; Stein, A. *Science* **1998**, 281, 538.
- (3) (a) Such, G. K.; Tjipito, E.; Postma, A.; Johnston, A. P. R.; Caruso, F. *Nano Lett.* **2007**, 7, 1706. (b) Zhu, Y.; Shi, J.; Shen, W.; Dong, X.; Feng, J.; Ruan, M.; Li, Y. *Angew. Chem., Int. Ed.* **2005**, 44, 5083.
- (4) (a) Buchold, D. H. M.; Feldmann, C. *Nano Lett.* **2007**, 7, 3489. (b) Chen, J.; Saeki, F.; Wiley, B. J.; Cang, H.; Cobb, M. J.; Li, Z. Y.; Au, L.; Zhang, H.; Kimmey, M. B.; Li, X. D.; Xia, Y. *Nano Lett.* **2005**, 5, 473.
- (5) Zelikin, A. N.; Li, Q.; Caruso, F. *Angew. Chem., Int. Ed.* **2006**, 45, 7743.
- (6) (a) Aguirre, C. I.; Reguera, E.; Stein, A. *Adv. Funct. Mater.* **2010**, 20, 2565. (b) Zakhidov, A. A.; Baughman, R. H.; Iqbal, Z.; Cui, C.; Khayrullin, I.; Dantas, S. O.; Marti, J.; Ralchenko, V. G. *Science* **1998**, 282, 897.
- (7) Wang, Z.; Li, F.; Ergang, N. S.; Stein, A. *Chem. Mater.* **2006**, 18, 5543.
- (8) Lee, K. T.; Lytle, J. C.; Ergang, N. S.; Oh, S. M.; Stein, A. *Adv. Funct. Mater.* **2005**, 15, 547.
- (9) Chen, X.; Wang, L.; Wen, Y.; Zhang, Y.; Wang, J.; Song, Y.; Jiang, L.; Zhu, D. *J. Mater. Chem.* **2008**, 18, 2262.
- (10) (a) Kuo, C.-W.; Shiu, J.-Y.; Wei, K. H.; Chen, P. J. *Chromatogr. A* **2007**, 1162, 175. (b) Wang, Y.; Caruso, F. *Adv. Funct. Mater.* **2004**, 14, 1012. (c) Choi, S.-W.; Xie, J.; Xia, Y. *Adv. Mater.* **2009**, 21, 2997. (d) Liu, Y.; Wang, S.; Lee, J. W.; Kotov, N. A. *Chem. Mater.* **2005**, 17, 4918. (e) Nakamura, R.; Kai, F.; Okamoto, A.; Newton, G. J.; Hashimoto, K. *Angew. Chem., Int. Ed.* **2009**, 48, 508.
- (11) (a) Zhang, Y. S.; Regan, K. P.; Xia, Y. *Macromol. Rapid Commun.* **2013**, 34, 485. (b) Lee, Y.; Park, S.; Lim, T. G.; Koh, W. G. *Biosense Bioelectron.* **2012**, 35, 243.

- (12) (a) Stein, A.; Li, F.; Denny, N. R. *Chem. Mater.* **2008**, *20*, 649. (b) Dong, A.; Wang, Y.; Tang, Y.; Zhang, Y.; Ren, N.; Gao, Z. *Adv. Mater.* **2002**, *14*, 1506. (c) Chai, G. S.; Shin, I. S.; Yu, J.-S. *Adv. Mater.* **2004**, *16*, 2057.
- (13) Kim, Y.; Cho, C.-Y.; Kang, J.-H.; Cho, Y.-S.; Moon, J. H. *Langmuir* **2012**, *28*, 10543.
- (14) Sanders, A. E.; Shah, P. S.; Sigman, M. B., Jr.; Hanrath, T.; Hwang, H. S.; Lim, K. T.; Johnston, K. P.; Korgel, B. A. *Nano Lett.* **2004**, *4*, 1943.
- (15) Cossagneau, T.; Caruso, F. *Adv. Mater.* **2002**, *14*, 1837.
- (16) (a) Wang, Z.; Stein, A. *Chem. Mater.* **2008**, *20*, 1029. (b) Wang, Z.; Ergang, N. S.; Al-Daous, M. A.; Stein, A. *Chem. Mater.* **2005**, *17*, 6805. (c) Kang, D. Y.; Kim, S.-O.; Chae, Y. J.; Lee, J. K.; Moon, J. H. *Langmuir* **2013**, *29*, 1192. (d) Wang, Z.; Kiesel, E. R.; Stein, A. J. *Mater. Chem.* **2008**, *18*, 2194.
- (17) (a) Kuang, D.; Brezesinski, T.; Smarsly, B. J. *Am. Chem. Soc.* **2004**, *126*, 10534. (b) Sel, O.; Kuang, D.; Thommes, M.; Smarsly, B. *Langmuir* **2006**, *22*, 2311.
- (18) Zhang, H.; Yu, X.; Braun, P. *Nat. Nanotechnol.* **2011**, *6*, 277.
- (19) Li, H.; Chang, L.; Wang, J.; Yang, L.; Song, Y. J. *Mater. Chem.* **2008**, *18*, 5098.
- (20) (a) Yu, J.-S.; Lee, S. J.; Yoon, S. B. *Mol. Cryst. Liq. Cryst. Sci. Technol., Sect. A* **2001**, *371*, 107. (b) Su, F.; Zhao, X. S.; Wang, Y.; Zheng, J.; Zhou, Z.; Lee, J. Y. *J. Phys. Chem. B* **2005**, *109*, 20200. (c) Perpall, M. W.; Perera, K. P. U.; DiMaio, J.; Ballato, J.; Foulger, S. H.; Smith, D. W., Jr. *Langmuir* **2003**, *19*, 7153. (d) Baumann, T. F.; Satcher, J. H., Jr. *J. Non-Cryst. Sol.* **2004**, *350*, 120.
- (21) Sun, H.; He, W.; Zong, C.; Lu, L. *ACS Appl. Mater. Interfaces* **2013**, *5*, 2261.
- (22) (a) Sun, X.; Li, Y. *Angew. Chem., Int. Ed.* **2004**, *43*, 597. (b) Titirici, M.-M.; White, R. J.; Falco, C.; Sevilla, M. *Energy Environ. Sci.* **2012**, *5*, 6796. (c) Titirici, M.-M.; Antonietti, M. *Chem. Soc. Rev.* **2010**, *39*, 103. (d) Falco, C.; Baccile, N.; Titirici, M.-M. *Green Chem.* **2011**, *13*, 3273.
- (23) Kubo, S.; Cakan, R. D.; Zhao, L.; White, R. J.; Titirici, M.-M. *ChemSusChem* **2010**, *3*, 188.
- (24) Kubo, S.; White, R. J.; Yoshizawa, N.; Antonietti, M.; Titirici, M.-M. *Chem. Mater.* **2011**, *23*, 4882.
- (25) White, R. J.; Yoshizawa, N.; Antonietti, M.; Titirici, M.-M. *Green Chem.* **2011**, *13*, 2428.
- (26) White, R. J.; Tauer, K.; Antonietti, M.; Titirici, M.-M. *J. Am. Chem. Soc.* **2010**, *132*, 17360.
- (27) (a) Tang, K.; White, R. J.; Xiaoke, M.; Titirici, M.-M.; van Aken, P. A.; Maier, J. *ChemSusChem* **2012**, *5*, 400. (b) Tang, K.; Fu, L.; White, R. J.; Yu, L.; Titirici, M. M.; Antonietti, M.; Maier, J. *Adv. Energy Mater.* **2012**, *7* (2), 873.
- (28) (a) Evans, D. F.; Wennerstroem, H. *The Colloidal Domain*, 2nd ed.; Wiley-VCH: Weinheim, Germany, 1999. (b) Louguet, S.; Kumar, A. C.; Sigaud, G.; Duguet, E.; Lecommandoux, S.; Schatz, C. J. *Colloid Interface Sci.* **2011**, *359*, 413. (c) Wind, B.; Killmann, E. *Colloid Polym. Sci.* **1998**, *276*, 903.
- (29) (a) Ishizuka, N.; Minakuchi, H.; Nakanishi, K.; Soga, N.; Tanaka, N. *J. Chromatogr., A* **1998**, *797*, 133. (b) Motokawa, M.; Kobayashi, H.; Ishizuka, N.; Minakuchi, H.; Nakanishi, K.; Jinnai, H.; Hosoya, K.; Ikegami, T.; Tanaka, N. *J. Chromatogr., A* **2002**, *961*, 53. (c) Tanaka, N.; Kobayashi, H.; Nakanishi, K.; Minakuchi, H.; Ishizuka, N. *Anal. Chem.* **2001**, *421A*. (d) Radisill, S. G.; Hein, N. M.; Terzic, D.; Stein, A. *Chem. Mater.* **2013**, *25*, 745.
- (30) Tauer, K.; Mueller, H. *Colloid Polym. Sci.* **2003**, *281*, 52.
- (31) Kubo, S.; Tan, I.; White, R. J.; Antonietti, M.; Titirici, M.-M. *Chem. Mater.* **2010**, *22*, 6590.
- (32) Lin, Y.; Alexandridis, P. *J. Phys. Chem. B* **2002**, *106*, 10834.
- (33) Giesche, H. *Part. Part. Syst. Charact.* **2006**, *23*, 1.
- (34) Ravikovitch, P. I.; Neimark, A. V. *Langmuir* **2002**, *18*, 9830.
- (35) (a) Meng, X.; Cui, H.; Dong, J.; Zheng, J.; Zhu, Y.; Wang, Z.; Zhang, J.; Jia, S.; Zhao, J.; Zhu, Z. *J. Mater. Chem. A* **2013**, in press. (b) Wang, Y.; Zheng, M.; Lu, H.; Feng, S.; Ji, G.; Cao, J. *Nanoscale Res. Lett.* **2010**, *5*, 913.
- (36) Yu, L.; Falco, C.; Weber, J.; White, R. J.; Howe, J. Y.; Titirici, M.-M. *Langmuir* **2012**, *28*, 12373.
- (37) Gandini, A. *Polym. Chem.* **2010**, *1*, 245.
- (38) Titirici, M.-M.; Antonietti, M.; Baccile, N. *Green Chem.* **2008**, *10*, 1204.
- (39) Falco, C.; Caballero, F. P.; Babonneau, F.; Gervais, C.; Laurent, G.; Titirici, M.-M.; Baccile, N. *Langmuir* **2011**, *27*, 14460.
- (40) As compared to the electrical conductivity of 160 S m⁻¹ measured for commercial carbon black "Denka Black" (Denki Kagaku Kogyo Co.) made by thermal decomposition of acetylene. Preparation of pellets was the same as mentioned in the Experimental Section.
- (41) Kaji, H.; Nakanishi, K.; Soga, N. *J. Sol-Gel Sci. Technol.* **1993**, *1*, 35.
- (42) Cosgrove, T. *Colloid Science—Principles, Methods and Application*; Blackwell Publishing: Oxford, U.K., 2005.
- (43) Wen, Y. H.; Lin, P.-C.; Lee, C. Y.; Hua, C. C.; Lee, T.-C. *J. Colloid Interface Sci.* **2010**, *349*, 134.
- (44) Gornowich, D. B.; Blanchard, G. J. *J. Phys. Chem. C* **2012**, *116*, 12165.